probably caused by charge traps that screened the influence of the gate.

An alternative method to achieve an exponential dependence of the tunneling current on gate voltage would be to use a barrier dielectric with a smaller Δ, which would be comparable with typical E_F realizable in graphene. One of such candidate materials is MoS_2, which has a band gap of about 1.3 eV and can be obtained in a mono- or few-layers state similar to hBN and graphene (*21*). Our first graphene-MoS_2–based devices demonstrate ON-OFF ratio close to 10.000 (fig. S5), which is sufficient for certain types of logic circuits.

We conclude that our tunneling devices offer a viable route for high-speed graphene-based analog electronics. The ON-OFF ratios already exceed those demonstrated for planar graphene FETs at room temperature by a factor of 10 (*3*–*7*). The transit time for the tunneling electrons through the nanometer-thick barriers is expected to be extremely fast (a few femtoseconds) (*13*–*17*) and exceeds the electron transit time in submicrometer planar FETs. It should also be possible to decrease the lateral size of the tunneling FETs down to the 10 nm scale, a requirement for integrated circuits. Furthermore, there appears to be no fundamental limitation to further enhancement of the ON-OFF ratios by optimizing the architecture and by using higher-quality gate dielectrics and, in particular, lower tunnel barriers (Δ < maximum achievable E_F).

References and Notes

1. P. Avouris, Z. H. Chen, V. Perebeinos, *Nat. Nanotechnol.* **2**, 605 (2007).
2. A. K. Geim, *Science* **324**, 1530 (2009).
3. F. Schweirz, *Nat. Nanotechnol.* **5**, 487 (2010).
4. Y. Wu *et al.*, *Nature* **472**, 74 (2011).
5. L. Liao *et al.*, *Nature* **467**, 305 (2010).
6. S. J. Han *et al.*, *Nano Lett.* **11**, 3690 (2011).
7. Y. M. Lin *et al.*, *Science* **332**, 1294 (2011).
8. E. V. Castro *et al.*, *Phys. Rev. Lett.* **99**, 216802 (2007).
9. J. B. Oostinga, H. B. Heersche, X. Liu, A. F. Morpurgo, L. M. K. Vandersypen, *Nat. Mater.* **7**, 151 (2008).
10. M. Y. Han, B. Ozyilmaz, Y. B. Zhang, P. Kim, *Phys. Rev. Lett.* **98**, 206805 (2007).
11. C. Stampfer *et al.*, *Front. Phys.* **6**, 271 (2011).
12. D. C. Elias *et al.*, *Science* **323**, 610 (2009).
13. S. Luryi, *Appl. Phys. Lett.* **52**, 501 (1988).
14. M. Heiblum, M. V. Fischetti, *IBM J. Res. Develop.* **34**, 530 (1990).
15. J. A. Simmons *et al.*, *J. Appl. Phys.* **84**, 5626 (1998).
16. A. Zaslavsky *et al.*, *Appl. Phys. Lett.* **83**, 1653 (2003).
17. A. Sciambi *et al.*, *Phys. Rev. B* **84**, 085301 (2011).
18. Materials and methods are available as supporting material on *Science* Online.
19. C. R. Dean *et al.*, *Nat. Nanotechnol.* **5**, 722 (2010).
20. A. S. Mayorov *et al.*, *Nano Lett.* **11**, 2396 (2011).
21. K. S. Novoselov *et al.*, *Proc. Natl. Acad. Sci. U.S.A.* **102**, 10451 (2005).
22. L. A. Ponomarenko *et al.*, *Nat. Phys.* **7**, 958 (2011).
23. R. V. Gorbachev *et al.*, *Small* **7**, 465 (2011).
24. A. H. Castro Neto, F. Guinea, N. M. R. Peres, K. S. Novoselov, A. K. Geim, *Rev. Mod. Phys.* **81**, 109 (2009).
25. J. G. Simmons, *J. Appl. Phys.* **34**, 1793 (1963).
26. E. L. Wolf, *Principles of Electron Tunneling Spectroscopy* (Oxford Univ. Press, Oxford, 1985).
27. L. A. Ponomarenko *et al.*, *Phys. Rev. Lett.* **105**, 136801 (2010).
28. J. M. Xue *et al.*, *Nat. Mater.* **10**, 282 (2011).
29. N. Kharche, S. K. Nayak, *Nano Lett.* **11**, 5274 (2011).
30. Y. N. Xu, W. Y. Ching, *Phys. Rev. B* **44**, 7787 (1991).

Acknowledgments: This work was supported by the European Research Council, European Commision FP7, Engineering and Physical Research Council (UK), the Royal Society, U.S. Office of Naval Research, U.S. Air Force Office of Scientific Research, and the Körber Foundation. A.M. acknowledges support from the Swiss National Science Foundation.

Supporting Online Material

www.sciencemag.org/cgi/content/full/science.1218461/DC1
Materials and Methods
SOM Text
Figs. S1 to S5
References (*31*–*35*)

27 December 2011; accepted 23 January 2012
Published online 2 February 2012;
10.1126/science.1218461

The Local Structure of Amorphous Silicon

M. M. J. Treacy[1]* and K. B. Borisenko[2,3]

It is widely believed that the continuous random network (CRN) model represents the structural topology of amorphous silicon. The key evidence is that the model can reproduce well experimental reduced density functions (RDFs) obtained by diffraction. By using a combination of electron diffraction and fluctuation electron microscopy (FEM) variance data as experimental constraints in a structural relaxation procedure, we show that the CRN is not unique in matching the experimental RDF. We find that inhomogeneous paracrystalline structures containing local cubic ordering at the 10 to 20 angstrom length scale are also fully consistent with the RDF data. Crucially, they also matched the FEM variance data, unlike the CRN model. The paracrystalline model has implications for understanding phase transformation processes in various materials that extend beyond amorphous silicon.

Amorphous silicon (a-Si) can be regarded as a classic example of a disordered four-coordinated covalent material. Understanding its structure has implications for understanding structures and structure-properties correlations not only for similar covalently bonded networks but also for a wider range of other amorphous materials. In general, having the correct structural model of an amorphous state is important in order to understand the structural origins of glass transitions and associated phenomena. Previous studies rely on spatially heterogeneous dynamics using either crystalline (*1*, *2*) or noncrystalline (*3*, *4*) inhomogeneities to explain kinetics of glass transitions and phenomena of glass-forming ability. Such knowledge is essential for a number of industrially important materials, such as phase-change memory materials for information storage (*5*, *6*). Accurate structural models are crucial for understanding mechanisms of deformation in metallic glasses (*7*). This knowledge is needed to ultimately build novel materials with the required properties. It is widely believed that the structure of a-Si is well represented by the continuous random network (CRN) model, which was first introduced by Zachariasen as a model for network glasses (*8*). The ideal CRN for a-Si is a fully four-coordinated, nonperiodic structure that is metastable with respect to crystalline silicon and is constructed primarily from five-, six- and seven-membered rings. Crystalline Si comprises six-membered rings only. High-quality CRN models, which reproduce the experimental density, have been developed by applying bond-swapping algorithms (*9*, *10*), in conjunction with framework relaxation using appropriate potentials (*11*, *12*). The models generate a reduced density function (RDF) that matches the essential features of experimental data obtained by high-energy x-ray and neutron diffraction (*13*), as well as electron diffraction (*14*). In addition, the models broadly reproduce features observed in Raman spectra (*15*), as well as the vibrational density of states obtained by neutron diffraction (*12*, *16*).

Other models for a-Si have been proposed. The paracrystallite model of Hosemann and Baggchi (1962) (*17*) and the microcrystallite model of Turnbull and Polk (1972) (*18*) are generally discredited because they are thought to be inconsistent with RDF data. Both models describe materials containing small grains of ordered material that are just a few nanometers in extent, but in the paracrystallite model there are strain gradients throughout the grains. The width of the second peak in the RDF suggests a range of Si-Si-Si angles that is thought to be inconsistent with either type of crystalline order. However, it has been argued that fluctuation electron microscopy (FEM) data provide irrefutable evidence for the presence of substantial topological crystallinity in a-Si at the 10 to 20 Å length scale (*19*). Although the FEM evidence has been reproduced by several groups for various samples of a-Si that were amorphized by different methods (*20*–*22*), the presence of topologically crystalline ordering in a-Si is not widely accepted as it appears to contradict carefully conducted RDF experiments (*13*). It has been asserted that claims

[1]Department of Physics, Arizona State University, Tempe, AZ 85287, USA. [2]Department of Materials, University of Oxford, Parks Road, Oxford OX1 3PH, UK. [3]Research Complex at Harwell, Rutherford Appleton Laboratory, Harwell Oxford, Didcot OX11 0FA, UK.

*To whom correspondence should be addressed. E-mail: treacy@asu.edu

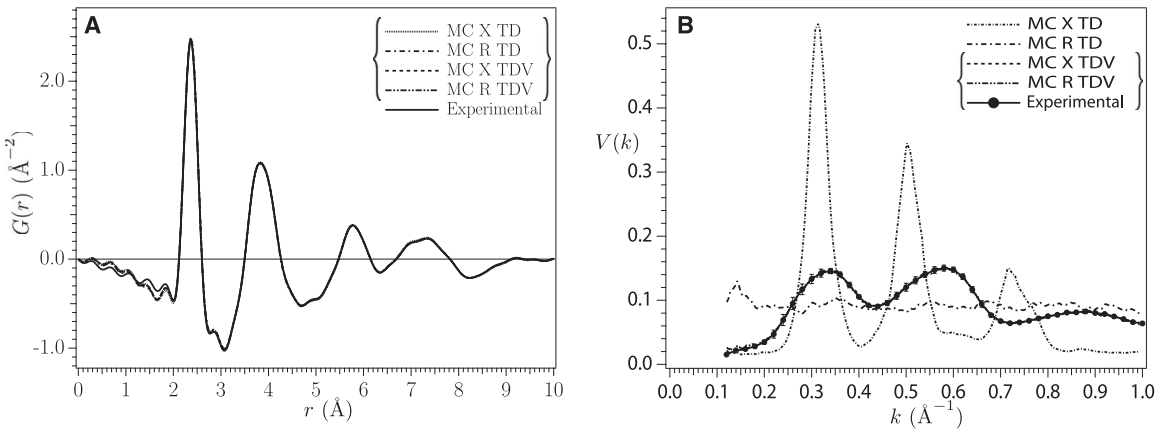

Fig. 1. (**A**) Reduced density functions, $G(r)$, obtained for an a-Si specimen and computed for four models by a Monte Carlo (MC) procedure using the experimental diffraction (D) and variance (V) data as a constraint. Both crystalline (X) and random (R) starting structures were used. A Tersoff potential (T) was applied as an additional constraint. (**B**) Variance plots, $V(k)$, for the experiment and four models. The braces, {}, in the legend indicate those traces that overlap.

Table 1. Selected structural and energetic properties of the four a-Si models. See text for details.

Model	U (eV/Si)	$R_{3\%}$	$R_{6\%}$	N_C	N_2	N_p
MC X TD	−3.99	0.2	84.6	3.58	611	281
MC R TD	−3.65	6.6	23.1	3.67	111	0
MC X TDV	−3.95	0.3	82.6	3.59	419	94
MC R TDV	−3.73	5.8	61.8	3.74	367	82

of longer-range order in glasses are unjustified because the random models, such as the CRN, account for all the observed features (*23*). We point out that although matching diffraction data are a necessary criterion for any successful model, alone it is not sufficient to identify a unique model. There exist topologically distinct homometric structures that also match the RDF data.

Experimentally, a-Si typically has a density about 1 to 2% less than that of the cubic crystalline phase. The area under the first-nearest neighbor peak of the RDF, $G(r)$, shows that a-Si has a coordination number less than 4, typically about 3.8 (*13*), which would account for the reduced density. Transmission electron microscopy (TEM) evidence shows that voids can occur in a-Si (*24*). Further, an experimentally constrained molecular relaxation (ECMR) study by Biswas *et al*. (*25*), using both diffraction (RDF) and FEM diffraction variance data as constraints, was found to support the void model. The implication is that a-Si can be described satisfactorily by an interrupted CRN model, with no topological order necessary to explain the data. However, the topology of the Biswas void model was not examined. The voids were introduced artificially, and it can be argued that the free void surfaces provide nucleation sites for paracrystallinity, which would explain the match to the FEM data.

Here we use a procedure similar to ECMR, but with a Tersoff atomic potential applied as an additional constraint. We show that refinements, made without introducing additional bias, yield inhomogeneous models containing topological crystallinity at the 10 to 20 Å length scale, with no voids, that are fully consistent with both the RDF and FEM data.

A serious deficiency of the ideal CRN model is that it is inconsistent with the FEM data (*19*). FEM examines the variability in microdiffraction patterns from small volumes of the sample, typically with probes of width $R \approx 10$ to 20 Å. The RDF and FEM techniques are complementary; the RDF method informs us about the mean diffraction, and FEM informs us about the variability of that diffraction from subregions of the sample. The RDF, being a volume-averaging technique, is insensitive to details about sample inhomogeneities. FEM microdiffraction simulations across CRN models (with 10 to 60 Å probes) confirm that different regions are qualitatively similar, as revealed by the featureless normalized variance of the microdiffraction pattern intensities. The normalized variance is obtained from the set of microdiffraction pattern intensities, $I(\boldsymbol{r}_p, \boldsymbol{k}, R)$, via

$$V(\boldsymbol{k},R) = \frac{\langle I^2(\boldsymbol{r}_p,\boldsymbol{k},R)\rangle_{r_p}}{\langle I(\boldsymbol{r}_p,\boldsymbol{k},R)\rangle^2_{r_p}} - 1 \qquad (1)$$

$\boldsymbol{r}_p$ is the location of the probe of width R (spatial resolution), and the angular brackets represent the averaging over all probe locations. For probe widths $R \geq 10$ Å, the two-dimensional variance pattern $V(\boldsymbol{k}, R)$ computed for typical CRN models is essentially flat, confirming that there are no special structural periodicities corresponding to a scattering vector $\boldsymbol{k}$. However, experimental FEM variance patterns from many different a-Si samples always show peaks near the 111, 200, 220, and 311 locations of the cubic Si structure. This indicates that there is crystalline topology present at length scales $R = 10$ to 20 Å. For larger probes, $R > 30$ Å, the variance fades as the probed width exceeds the typical correlation length. A recent correlograph study of such patterns (*22*) confirms this interpretation of inhomogeneity in a-Si.

Large models containing N atoms, and therefore $3N$ coordinate degrees of freedom, are underconstrained by electron diffraction data, which typically comprise about 400 experimental points after radial averaging. This underconstraint creates a broad solution space of homometric structures—those that will reproduce the diffraction intensity—even when models are additionally constrained by appropriate potentials for a-Si. The CRN itself is not a unique structure; there are many topologically equivalent arrangements. Thus, the solution space will be amply populated with similar CRN structures. However, CRN models are not the only viable structural arrangement consistent with diffraction data. The solution space is further confined when FEM data are added as constraints. When this is done, we find that CRN structures are excluded as solutions.

We recently applied an experimentally constrained structural relaxation (ECSR) computational procedure (*26*), closely similar to the ECMR method of Biswas *et al.* (*27*, *28*), to search for structural solutions for four different types of a-Si using electron diffraction data and FEM variance data (*26*). For each structural configuration, the ECSR algorithm evaluates a cost function that contains three terms: (i) the Tersoff potential, U, for the silicon model (*29*); (ii) the integrated square difference of the experimental and computed reduced electron diffraction intensities $\varphi(k)$ in the range $0 \leq k \leq 2.5$ Å^{-1}; and (iii) the integrated square difference of the experimental and computed FEM variance $V(k)$ in the range $0.12 \leq k < 1.0$ Å^{-1}. Variance calculations assume a probe size (resolution) of 10 Å. The x,y,z coordinates of a randomly selected atom are adjusted by a small random amount, and the cost function is reevaluated. The move is accepted or rejected via the Metropolis algorithm (*30*). The diffraction and variance costs were weighted relative to the Tersoff potential so that the typical changes in all three terms, arising from random atom moves, were approximately equal. Details of our experimental and

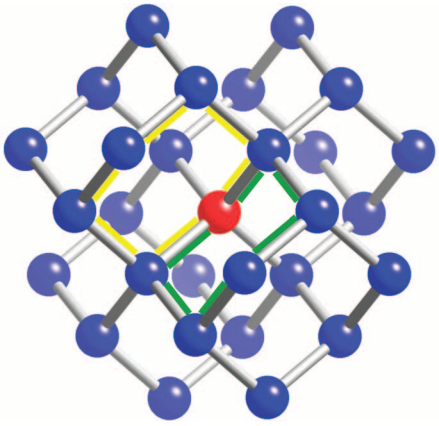

Fig. 2. The 29-atom local cluster for crystalline cubic silicon. The central atom (red) has four bonds and six possible intervertex angles. There are two six-membered rings spanning each intervertex angle (yellow and green paths), giving it a vertex symbol $6_2 \cdot 6_2 \cdot 6_2 \cdot 6_2 \cdot 6_2 \cdot 6_2$. This 9 Å diameter unit provides a convenient minimal topological description for a paracrystalline cluster. In real materials, strain may deform it from this idealization without altering the bonded topology. Local clusters for the CRN will contain some five-membered rings.

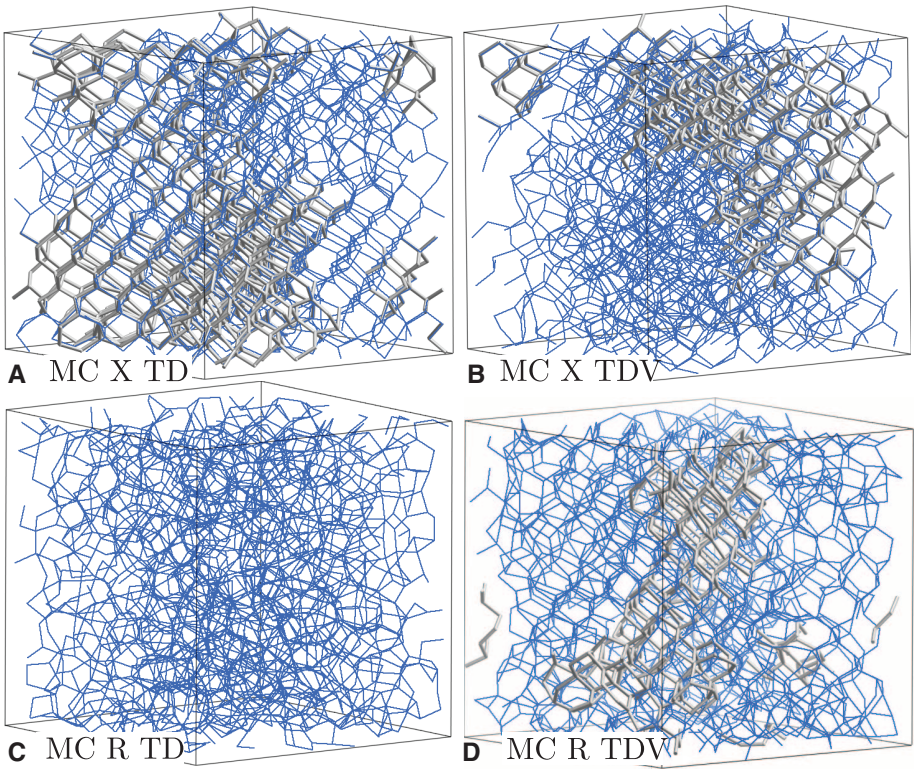

Fig. 3. (**A** to **D**) The four 1728-atom models, after structural relaxation, viewed as periodic networks. The atoms connected by gray bonds represent topologically cubic-Si regions. All four models give essentially identical $G(r)$ plots (Fig. 1A).

computational methods are described elsewhere (*26*, *31*, *32*).

Results for an a-Si sample that was amorphized by implantation of high-energy Si ions are presented here. The experimental RDF, $G(r)$, obtained from electron diffraction, is presented in Fig. 1A along with the simulated $G(r)$ plots for four different ECSR runs. Both crystalline (X) and random (R) starting configurations were used. For each of these there were two runs: one with electron diffraction only as an experimental constraint (i.e., the variance weight was set to zero); the second with the experimental variance included. All four runs included the Tersoff potential. The notable feature of these five plots is that they are essentially identical. Yet, the structural topology of each model is substantially different, as revealed by the variance simulations for each model (Fig. 1B). For the two simulations that were not constrained by the variance (labeled "MC X TD" and "MC R TD"), the resulting variance plots are markedly different. For the crystalline starting configuration, strong variance peaks arise, indicating substantial inhomogeneity persisting in the final model. For the random starting configuration, the variance curve is essentially flat, indicating a homogeneous structure. It has a high density of three-membered rings, and so is appreciably different from an ideal CRN, which has mostly five-, six-, and seven-membered rings. Neither plot matches the variance data. The two plots for the models that were constrained by the variance data (labeled "MC X TDV" and "MC R TDV") match the experimental variance perfectly. Despite the dissimilarity of the starting structures, these two models are topologically similar. The model properties are summarized in Table 1.

Models that started from a crystalline configuration (X) have the lowest Tersoff energies U and retain the highest densities of six-membered rings, R_6. Conversely, the models that were seeded by a random, CRN-like structure have higher Tersoff energies, and substantially lower densities of six-membered and more three-membered rings, R_3. The average coordination numbers, N_C, were about the same for each model, ~3.6 for the crystal-seeded models and ~3.7 for the random-seeded models, assuming a maximum bond length of 2.7 Å. N_C rises to ~3.8 when estimated from the area under the first peak of $G(r)$. A crude measure of latent crystalline coordination is obtained by examining the coordination sequences for each Si atom in the models. Cubic (and hexagonal) silicon has a coordination sequence that begins 1-4-12, out to the second shell. The parameter N_2 reports the number of Si atoms in the model that have this sequence. An atom with this sequence is not necessarily part of a topologically crystalline environment, but if it does not have this sequence, then it is clearly not in a topologically crystalline environment. A more reliable indicator of extensive crystalline topology, 10 Å and wider, is the atomic vertex symbol, which delineates a local cluster (*33*, *34*). This gives the size and number of rings at each of the six intervertex angles of a tetrahedrally coordinated silicon atom. Both cubic and hexagonal Si have vertex symbols $6_2 \cdot 6_2 \cdot 6_2 \cdot 6_2 \cdot 6_2 \cdot 6_2$, meaning that there are two distinct six-membered ring paths through each silicon atom and any two of its bonded neighbors. In crystalline cubic Si, there are 29 atoms involved in the local cluster that spans the vertex symbol, forming a unit that is ~9 Å in diameter (Fig. 2). The two models that were started as crystals both contain a substantial number of paracrystalline Si local clusters. In the table, N_p is the number of atoms that have the topologically cubic vertex symbol. Curiously, the model that was not constrained by the variance ("MC X TD") has approximately three times as much topological crystallinity as the variance-constrained model ("MC X TDV").

All four models are equally "diffraction amorphous." Both the "MC X TDV" (Fig. 3B) and the "MC R TDV" (Fig. 3D) models reproduce both the experimental $G(r)$ and $V(k)$ plots and converge to topologically similar structures. Because electron selected-area diffraction patterns are averaged over large areas, they show rotational homogeneity, whereas microdiffraction patterns show considerable spatial inhomogeneity. The inhomogeneous structures shown in Fig. 3, B and D, therefore appear to represent the real material better. The structure is not 100% ordered; only about 10 to 15% of the atoms must be associated with the topological ordering to reproduce the variance data. The remaining material is not topologically crystalline. Annealing reduces the amplitude of the variance peaks in this sample by about half, which reduces the extent of the paracrystalline ordering, but does not eliminate it (*26*).

An important difference between x-ray studies and FEM studies is the sample thickness. For FEM studies, the film should be less than about 300 Å, whereas in x-ray studies films can be substantially thicker, ~10 μm. As is true for all electron microscopy studies, structural artifacts at the film surfaces may affect results. Careful studies of a-Si samples in both plan view and cross-section view do not show any difference between surfaces and bulk. The thickness dependence of the variance signal from a-Si has been studied carefully, and it does not behave as a constant surface artifact (*21*, *35*). The FEM variance curves for a-Si have been consistently reproduced by several groups for a variety of a-Si samples prepared by different methods (*19*, *21*, *31*, *35*).

Amorphous silica, and some types of evaporated amorphous carbon, do show essentially flat variance curves that are consistent with a CRN (*36*, *37*). Recent evidence shows that ordered regions can persist in pressure- and temperature-amorphized silica glasses (*38*). Although the combination of the FEM variance data with the RDF data substantially narrows the available solution-space, the precise structural configuration of the inhomogeneity is still not established, although it appears most likely to be of paracrystalline type. More detailed models will require enhancements of the ECSR method as well as improved methods for modeling the scattering decoherence (related to inelastic scattering events), which affects the variance more strongly than the mean diffraction. Valuable additional information would be provided by application of variable-resolution FEM and correlograph analysis, where angular correlations in scattering are studied as a function of the probe size (*21*, *22*, *35*).

Because every a-Si sample studied by FEM to date, by several groups, shows distinctive variance peaks of the type associated with paracrystallinity, we conclude that they are all inhomogeneous at the 10 to 20 Å length scale, consistent with the paracrystallite model of Hosemann and Baggchi (*17*). Notwithstanding the RDF data, these samples do not agree with the ideal CRN model, which we conclude is a structural idealization that is not realized in practical a-Si thin films. Our conclusions regarding pervasive, heterogeneous, medium-range order in a-Si have implications for a wide variety of amorphous materials in general that have been studied by diffraction alone.

References and Notes

1. U. R. Pedersen, T. B. Schrøder, J. C. Dyre, P. Harrowell, *Phys. Rev. Lett.* **104**, 105701 (2010).
2. H. Tanaka, T. Kawasaki, H. Shintani, K. Watanabe, *Nat. Mater.* **9**, 324 (2010).
3. N. Jakse, A. Pasturel, *Appl. Phys. Lett.* **93**, 113104 (2008).
4. Y. Q. Cheng, H. W. Sheng, E. Ma, *Phys. Rev. B* **78**, 014207 (2008).
5. B.-S. Lee *et al.*, *Science* **326**, 980 (2009).
6. T. H. Lee, S. R. Elliott, *Phys. Rev. Lett.* **107**, 145702 (2011).
7. S. Pauly, S. Gorantla, G. Wang, U. Kühn, J. Eckert, *Nat. Mater.* **9**, 473 (2010).
8. W. H. Zachariasen, *J. Am. Chem. Soc.* **54**, 3841 (1932).
9. F. Wooten, K. Winer, D. Weaire, *Phys. Rev. Lett.* **54**, 1392 (1985).
10. G. T. Barkema, N. Mousseau, *Phys. Rev. B* **62**, 4985 (2000).
11. R. L. C. Vink, G. T. Barkema, W. F. van der Weg, N. Mousseau, *J. Non-Cryst. Solids* **282**, 248 (2001).
12. R. L. C. Vink, G. T. Barkema, M. A. Stijnman, R. H. Bisseling, *Phys. Rev. B* **64**, 245214 (2001).
13. K. Laaziri *et al.*, *Phys. Rev. B* **60**, 13520 (1999).
14. D. J. H. Cockayne, *Annu. Rev. Mater. Res.* **37**, 159 (2007).
15. R. L. C. Vink, G. T. Barkema, W. F. van der Weg, *Phys. Rev. B* **63**, 115210 (2001).
16. W. A. Kamitakahara, C. M. Soukoulis, H. R. Shanks, U. Buchenau, G. S. Grest, *Phys. Rev. B* **36**, 6539 (1987).
17. R. Hosemann, S. N. Baggchi, *Direct Analysis of Diffraction by Matter* (North-Holland, Amsterdam, 1962).
18. D. Turnbull, D. Polk, *J. Non-Cryst. Solids* **8-10**, 19 (1972).
19. M. M. J. Treacy, J. M. Gibson, P. J. Keblinski, *J. Non-Cryst. Solids* **231**, 99 (1998).
20. P. M. Voyles, J. E. Gerbi, M. M. J. Treacy, J. M. Gibson, J. R. Abelson, *Phys. Rev. Lett.* **86**, 5514 (2001).
21. S. N. Bogle, P. M. Voyles, S. V. Khare, J. R. Abelson, *J. Phys. Condens. Matter* **19**, 455204 (2007).
22. J. M. Gibson, M. M. J. Treacy, T. Sun, N. J. Zaluzec, *Phys. Rev. Lett.* **105**, 125504 (2010).
23. A. C. Wright, *Phys. Chem. Glasses Eur. J. Glass Sci. Technol. B* **49**, 103 (2008).
24. S. C. Moss, J. F. Graczyk, *Phys. Rev. Lett.* **23**, 1167 (1969).
25. P. Biswas, R. Atta-Fynn, D. A. Drabold, *Phys. Rev. B* **69**, 195207 (2004).
26. K. B. Borisenko *et al.*, *Acta Mater.* **60**, 359 (2012).
27. P. Biswas, D. Tafen, D. A. Drabold, *Phys. Rev. B* **71**, 054204 (2005).
28. J. Hwang, A. M. Clausen, H. Cao, P. M. Voyles, *J. Mater. Res.* **24**, 3121 (2009).
29. J. Tersoff, *Phys. Rev. B* **38**, 9902 (1988).
30. W. H. Press, S. A. Teukolsky, W. T. Vetterling, B. P. Flannery, *Numerical Recipes in C* (Cambridge Univ. Press, Cambridge, 1992).
31. B. Haberl *et al.*, *Phys. Rev. B* **79**, 155209 (2009).
32. See supporting material on *Science* Online.
33. C. S. Marians, L. W. Hobbs, *J. Non-Cryst. Solids* **124**, 242 (1990).
34. M. M. J. Treacy, P. M. Voyles, J. M. Gibson, *J. Non-Cryst. Solids* **266-269**, 150 (2000).
35. P. M. Voyles, D. A. Muller, *Ultramicroscopy* **93**, 147 (2002).
36. J. M. Gibson, J.-Y. Cheng, P. M. Voyles, M. M. J. Treacy, D. C. Jacobson, *Microstructural Processes in Irradiated Materials*, S. J. Zinkle, G. Lucas, R. Ewing, Eds. (Materials Research Society, Warrendale, PA, 1999), vol. 540, pp. 27–32.
37. G. Zhao, P. R. Buseck, A. Rougée, M. M. J. Treacy, *Ultramicroscopy* **109**, 177 (2009).
38. D. A. Keen, R. McGreevy, *Nature* **344**, 423 (1990).

Acknowledgments: M.M.J.T acknowledges support from the Leverhulme Trust and from the U.S. Department of Energy, Contract no. DE-PS02-09ER09-01. K.B.B. thanks the UK Engineering and Physical Sciences Research Council (grant EP/F048009/1) for support. We thank B. Haberl, J. S. Williams, J. E. Bradby, and A. C. Y. Liu for providing the data used in this report. The data used in this work have been presented previously in (*31*) and (*26*).

Supporting Online Material

www.sciencemag.org/cgi/content/full/335/6071/950/DC1
Materials and Methods
SOM Text
Tables S1 and S2
References (*39*–*44*)

3 October 2011; accepted 4 January 2012
10.1126/science.1214780

Satellite Estimates of Precipitation-Induced Dissipation in the Atmosphere

Olivier Pauluis[1,*] and Juliana Dias[2]

A substantial amount of frictional dissipation in the atmosphere occurs in the microphysical shear zones surrounding falling precipitation. The dissipation rate is computed here from recently available satellite retrieval from the Tropical Rainfall Measurement Missions and is found to average 1.8 watts per square meter between 30°S and 30°N. The geographical distribution of the precipitation-induced dissipation is closely tied to that of precipitation but also reveals a stronger dissipation rate for continental convection than for maritime convection. Because the precipitation-induced dissipation is of the same magnitude as the turbulent dissipation of the kinetic energy in the atmosphere, changes in the hydrological cycle could potentially have a direct impact on the amount of kinetic energy generated and dissipated by the atmospheric circulation.

Around each individual water droplet and ice crystal in the atmosphere, there is a microphysical flow that acts to slow down its fall. As a result, precipitation falls through the air at a terminal velocity determined by the balance between the gravitational acceleration and the aerodynamical drag exerted by the surrounding air. The effect of the drag is dramatic: The typical terminal velocity for a raindrop is about a few meters per second, which is two orders of magnitude smaller than the free-fall velocity it would attain in the absence of any drag force.

This drag also acts as damping mechanism that dissipates kinetic energy within the shear zones surrounding each individual hydrometeor (*1*). From a macroscopic perspective, a drag force $\mathbf{F}$ that acts on two different bodies moving at relative velocity $\mathbf{v_r}$ is associated with a net loss of mechanical energy equal to $\mathbf{F} \cdot \mathbf{v_r}$. For falling precipitation, the relative velocity is equal to the terminal velocity of the hydrometeors, v_T, where-

[1]Courant Institute of Mathematical Sciences, New York University, 251 Mercer Street, New York, NY 10012, USA. [2]Physical Sciences Division, Earth System Research Laboratory (ESRL)/National Oceanic and Atmospheric Administration (NOAA), Boulder, CO 80305, USA.

*To whom correspondence should be addressed. E-mail: pauluis@cims.nyu.edu